OPTIMIZED STILLINGER-WEBER POTENTIALS FOR 1H, 1T AND 1T′ PHASES OF WS_2 FOR MOLECULAR DYNAMICS STUDIES: THERMAL TRANSPORT AS AN EXAMPLE

A THESIS SUBMITTED TO

THE GRADUATE SCHOOL OF ENGINEERING AND SCIENCE

OF BILKENT UNIVERSITY

IN PARTIAL FULFILLMENT OF THE REQUIREMENTS FOR

THE DEGREE OF

MASTER OF SCIENCE

IN

PHYSICS

By

Alim Mohamed Waheed

January 2024

Optimized Stillinger-Weber Potentials for 1H, 1T and 1T′ Phases of WS_2 for Molecular Dynamics studies: Thermal Transport as an Example

By Alim Mohamed Waheed

January 2024

We certify that we have read this thesis and that in our opinion it is fully adequate, in scope and in quality, as a thesis for the degree of Master of Science.

Oğuz Gülseren(Advisor)

Mehmet Cemal Yalabık

Hande Tofolli

Approved for the Graduate School of Engineering and Science:

Orhan Arıkan
Director of the Graduate School

ABSTRACT

OPTIMIZED STILLINGER-WEBER POTENTIALS FOR 1H, 1T AND 1T′ PHASES OF WS_2 FOR MOLECULAR DYNAMICS STUDIES: THERMAL TRANSPORT AS AN EXAMPLE

Alim Mohamed Waheed
M.S. in Physics
Advisor: Oğuz Gülseren
January 2024

The advent of graphene has poured numerous amount of research effort into the study 2D materials and utilizing it for device fabrication. Monolayer Transition Metal Dichalcogenides are one such class of polymorphic material with high prospect in versatile device applications due to its unique properties exhibited across the various phases. Classical Molecular Dynamics is a powerful tool that can be utilized to study the thermal and mechanical properties of these phases. Considering this, we optimise Stillinger-Weber type Potential for the seperate 1H, 1T and 1T′ phases of WS_2 using Particle Swarm Optimization. These potentials are validated by comparison of phonon dispersion curves, Density Functional Theory (DFT) based target characteristic data and through an accuracy assessment conducted using Non-Equilibrium Molecular Dynamic (NEMD) simulations to evaluate thermal conductivity of the polymorphic structures. Thermal conductivity results obtained for 1H and 1T′ are in good agreement with first principle predictions calculated using Boltzmann Transport Equation. NEMD simulation of 1T phase prove to be challenging due to its dynamic instability with incoherent buckle structure formation along the symmetric directions.

Keywords: 2D Materials, Particle Swarm Optimization, Stillinger-Weber, Thermal Conductivity, Molecular Dynamics, Transition Metal Dichacogenides.

ÖZET

WS_2'NİN 1H, 1T VE 1T′ FAZLARI İÇİN OPTİMİZE EDİLMİŞ STILLINGER-WEBER POTANSİYELLERİ: TERMAL İLETİM ÖRNEĞİ

Alim Mohamed Waheed
Fizik, Yüksek Lisans
Tez Danışmanı: Oğuz Gülseren
Ocak 2024

Grafenin ortaya çıkışı, 2D malzemelerin araştırılması ve çıktıların cihaz üretimi için kullanılması konusunda birçok araştırma çabasına yol açmıştır. Tek katmanlı geçiş metali diklorojenitler, farklı fazlarda sergilediği benzersiz özellikler nedeniyle çok yönlü cihaz uygulamalarında yüksek potansiyele sahip olan polimorfik bir malzeme sınıfına örnektir. Klasik Moleküler Dinamik hesapları, bu fazların termal ve mekanik özelliklerini incelemek için kullanılabilecek güçlü bir araçtır. Bu bağlamda, Parçacık Sürü Optimizazyonu yardımıyla WS2'nin ayrı ayrı 1H, 1T ve 1T′ fazları için Stillinger-Weber tipi potansiyeli geliştirdik. Bu potansiyellerin doğruluk sağlaması, fonon dağılım eğrilerinin karşılaştırılması, Yoğunluk Fonksiyoneli Teorisi (YFT) ile hesaplanan karakteristik veriler ve polimorfik yapıların termal iletkenliğini değerlendirmek için yapılan "Non-Equilibrium Molecular Dynamic (NEMD)" simülasyonları kullanılarak gerçekleştirilmiştir. 1H ve 1T' için elde edilen termal iletkenlik sonuçları, Boltzmann Taşıma Denklemi kullanılarak hesaplanan birinci prensip tahminleri ile tutarlı uyum göstermektedir. 1T fazının "NEMD simülasyonu", simetrik şekilde oluşum gösteren tutarsız toka yapısıyla dinamik istikrarsızlığı nedeniyle zorlayıcı olduğu gösterilmiştir.

Anahtar sözcükler: 2D Malzemeleri, Parçacık Sürü Optimizasyonu, Stillinger-Weber, Termal İletkenlik, Moleküler Dinamikler, Geçiş metali diklorojenitler.

Acknowledgement

First and foremost, I would like to thank God, the Almighty for his countless blessings, for his mercy, grace and the strength throughout the most challenging of times.

I would like to express my sincere gratitude to my advisor Prof. Oğuz Gülseren for giving me this opportunity to study under his guidance, for his kind supervision and patience.

I would also like to thank my colleague and friend Muhammad Hilal for his help during my Masters thesis work and Dr. Arash Mobaraki for his technical insight and his PhD thesis which has helped me immensely in my work.

I would like to thank my closest friends whom I have spent most of my time in Bilkent with. Said, Furkan, Çiğdem and Ronak, have made my time in Bilkent a pleasent journey and an adventure.

I would like to extend my deepest gratitude and thanks for the my Maldivian friends Aslam, Naaz, Shazee and Nisha for making my entire stay in Türkiye homelike, hospitable and joyful.

Special thanks to Stafford sir and his family for their constant guidance, advice and kindness throughout everything in life.

A would like to specially thank all my family members for their love, kindness, support throughout every step of my life and without whom I would not have come this far in my higher education studies abroad. Their constant belief in my potential and encouragement has been essential in driving me forward throughout my studies.

The numerical calculations reported in this paper were partially performed at TUBITAK ULAKBIM, High Performance and Grid Computing Center.

Contents

List of Figures

List of Tables

Chapter 1

Introduction

Since the exfoliation of graphene [3] from its bulk counterpart graphite, 2D materials have gained a center-stage spotlight in nanodevice fabrication. One such class of 2D materials is Transition Metal Dichalcogenides (TMDs) with general chemical formula MX_2 where M and X denote transition metal and chalcogen elements. TMDs are layered materials formed in stacks of X-M-X layers with strong intra-layer bonding. Its weak inter-layer bonding in the bulk form allows them to be exfoliated into single monolayers [4]. Along with its low dimensionality and flexibility, monolayers of such materials are attractive due to their direct band-gap [5] property exhibited in its most stable form, which is important for applications such as transistor technologies [6, 7], sensing in photodetectors [8], electroluminescence [9] and photoluminescence [10, 11] in optoelectronic devices.

Monolayer TMDs also exhibit different structural phases based on X-M-X layer stacking sequence. Thermodynamically most stable 1H phase (P6m2 space-group) is a semiconductor and has a trigonal prismatic structure while the metastable 1T phase (P3m1 space group) is metallic and has six X atoms octahedrally bonded to the M atom. The semi-metallic 1T′ phase (P21/m space-group) has a distorted 1T structure with trimerized zigzag transition metal chains. In recent years there have been an increasing amount of interest in the exploitation of the unique properties of each polymorphic structure to fabricate more novel and

versatile devices. Recent studies show the prospect of using 1T and 1T′ TMDs in numerous applications such as development of supercapacitors [12], battery electrodes [13, 14] and thermoelectric devices [15].

Thermal and mechanical properties of such polymorph structures plays an important role in the device applications. Classical Molecular dynamics is a powerful tool that can be employed to investigate these properties in systems consisting of a large number of atoms since *ab initio* Molecular Dynamics can be computationally expensive. Furthermore, DFT analysis of phonon properties are constraint to zero temperature and solutions using Boltzmann Transport Equation are calculated with perfect crystal structures. Molecular Dynamics also provides an alternative with computational simulations where experimental procedures may prove to be infeasible or other factors such as sample quality and size may affect the experimental results.

Results using classical Molecular Dynamics is highly dependent on the ability of the interatomic potential to accurately describe the atomic interactions. Previous studies on molecular dynamics of TMDs have been mostly carried out using Interatomic Potentials optimized for the 1H phase [16, 17]. Studies have also been conducted which suggests the limited transferability of these potentials to the 1T and 1T′ phases [18]. According to the author's knowledge, there is no fully transferable potentials developed for use in all of the phases and this leaves much to be desired.

In this thesis, we optimize Stillinger-Weber type potential for the 1H, 1T and 1T′ polymorphic structures of monolayer TMD using WS_2 as a case-study. To assess the accuracy of the potentials, we investigate the thermal property by performing NEMD simulations to evaluate the thermal conductivity of each phase and compare it with first principles predictions obtained using Boltzmann Transport Equation. In the next chapter, we discuss in detail the background theory of Interatomic Potentials, the chosen optimization method for Stillinger-Weber Potential and computational methodology for thermal conductivity calculations.

Chapter 2

Theory and Computational Methods

2.1 Interatomic Potentials

Interatomic potentials (IP) are mathematical empirical models formulated to describe the interaction between atoms by the prediction of energy and classical forces. They are usually formulated as function of the atomic positions, which can be expressed as series sum of N-body contributions [19], i.e.

$$V = \sum_{i=1}^{N} V_1(\vec{r}_i) + \sum_{i,j=1}^{N} V_2(\vec{r}_i, \vec{r}_j) + \sum_{i,j,k=1}^{N} V_3(\vec{r}_i, \vec{r}_j, \vec{r}_k) + \cdots \tag{2.1}$$

The single particle term V_1 refers to the external forces applied on the individual atoms and V_2 term reflect the interaction of one atom with another. Higher order terms reflect the contribution of many body effects to the potential. The objective of formulating such potentials is to inexpensively describe these interatomic interactions which mimics the equivalent quantum mechanical systems to an acceptable degree of accuracy. The purpose of this is to reduce the computational cost of large-scale atomistic simulations since *ab initio* electronic structure methods are limited to systems with number of atoms on the order of $\sim 10^2$

and time scales of 100 picoseconds [20]. Hence, the current hardware limitations necessitates an accuracy-efficiency trade-off.

Various potentials have been developed in the course of last few decades out of which some potentials have been found to be very versatile and successful in describing multitude of single, binary and some higher order systems. Most of the widely used potentials for covalent bonded systems are Stillinger-Weber (SW) [19], Tersoff [21, 22, 23] and Brenner (REBO) Potentials [24]. In addition to this embedded-atom methods (EAM) potentials [25, 26] are used to describe interactions for metals and metal alloys.

In the last decade, a new class of IPs formulated using machine learning methods has emerged. Machine Learning Interatomic Potentials (MLIP) works by formulating a local structural descriptor of the atomic environment based on its position and neighbours. The descriptor serves as the argument of a regression model which gets mapped onto the Potential Energy Surface (PES). The main components which constitute the MLIPs are thus the descriptors, regression models and the PES reference data used to train the models. A multitude of descriptors has been proposed and implemented such as Gaussian [27, 28], Zernike [29], moment tensor [30], smooth overlap of atomic functions [31] and spectral neighbour analysis potential [32]. In addition to this, recent developments in the descriptors utilizes graph-based description where atoms are considered as nodes and bonds as edges [33]. The regression models used include artificial neural network [27], Gaussian process [34] and kernel ridge regression [35]. These regression models contain parameters typically on the order of 10^3 which are trained on PES data obtained using DFT or other electronic structure methods.

A highly desired characteristic in the both MLIP and traditional IP is its transferability. It is often understood as the flexibility of a potential to accurately predict or extrapolate the behaviour of a structure different from the dataset which it was fit to reproduce. For instance a more transferable potential for a crystal structure could be able to correctly describe its properties across multiple phases. Comparatively physically-informed MLIPs and traditional IPs have similar transferability [20]. The reliance of MLIPs on both large reference databases

and number of fitting parameters increase the computational cost in both training and simulations. Hence, traditional IPs still remain a good alternative to MLIPs.

2.1.1 Stillinger-Weber Potential

SW potential was originally developed to simulate solid and liquid phases of silicon [19]. SW potential includes a pair term ϕ_2 to describe the directional bonds and a threebody term ϕ_3 to describe the angular bonding which maintains the appropriate crystal structure and provides another degree of freedom to accurately model the PES from the configuration space. The mathematical form of the SW potential can be written as

$$E = \sum_i \sum_{j>i} \phi_2(r_{ij}) + \sum_i \sum_{j\neq i} \sum_{k>j} \phi_3(r_{ij}, r_{ik}, \theta_{ijk}) \tag{2.2}$$

$$\phi_2(r_{ij}) = A_{ij}\left[\frac{B_{ij}}{r_{ij}^4} - 1\right] \exp\left(\frac{\sigma_{ij}}{r_{ij} - r_{ij}^{max}}\right) \tag{2.3}$$

$$\begin{aligned}\phi_3(r_{ij}, r_{ik}, \theta_{ijk}) = \lambda_{ijk}\big[\cos\theta_{ijk} - \cos\theta_{0,ijk}\big]^2 \times \\ \exp\left(\frac{\gamma_{ij}\sigma_{ij}}{r_{ij} - r_{ij}^{max}}\right) \exp\left(\frac{\gamma_{ik}\sigma_{ik}}{r_{ik} - r_{ik}^{max}}\right)\end{aligned} \tag{2.4}$$

Here r_{ij}, r_{ik} describes the distance between atoms i, j and i, k respectively. θ_{ijk} is the angle between the atoms i, j and k where the vertex is formed at the atom i and $\theta_{0,ijk}$ is the equilibrium bond angle. The cutoff distance is given by r^{max} which greatly reduces the computational cost by the implementation of neighbour lists. A, B, σ, λ and γ are remaining parameters which needs to be case-specifically optimized.

A modified version of the SW potential has also been developed in order to include a cutoff function $f_C(\delta)$ to the threebody term [36]. In some crystal structures such as TMDs there are distinguishing three-body angles formed by the same types of atoms. To exclude the threebody potential from affecting unnecessary angles, f_C is multiplied with ϕ_3 in order for the energy and force contributions to smoothly decay to zero in the region $|\delta| > \delta_2$.

$$\delta = \cos\theta_{ijk} - \cos\theta_{0,ijk} \tag{2.5}$$

$$f_C(\delta) = \begin{cases} 1 & |\delta| < \delta_1 \\ \frac{1}{2} + \frac{1}{2}\cos\left(\pi \frac{|\delta| - \delta_1}{\delta_2 - \delta_1}\right) & \delta_1 < |\delta| < \delta_2 \\ 0 & \delta_2 < |\delta| \end{cases} \tag{2.6}$$

Since the development of SW potential, it has been used to study multiple materials such as Ge [37], semiconducting compounds composed of {Zn, Cd, Hg, S, Se, Te} [38], InAs and GaAs [39], tetrahedral carbon [40] and many others. Some of the recent studies on 2D materials such as silicene [41], phosphorene [42], borophene [43] and boron nitride [44] has also focused their works on developing better models using SW. TMDs has also been one of the 2D material class that has successfully incorporated SW to describe their mechanical and thermal properties [45, 46, 47, 48]. In this study we use SW potential given its versatility and relative transferability.

2.2 Particle Swarm Optimization

The Interatomic Potentials which describes how the atoms apply forces on each other as a function of atomic positions, needs to be correctly parameterized in order for the atoms to behave in accurate manner which will reproduce similar results to experimental data or DFT calculations and also predict new behaviour which it was not optimized to reproduce. Optimization of parameters for linear functional forms are guaranteed to converge to a global minimum/maximum since cost function manifold in the parameter phase space is concave/convex. However for complex functional forms which are usually nonlinear, the optimized parameters are not guaranteed to converge to a global best fit. This is because of the complexity of the geometric nature of the cost function manifold in these nonlinear models. Moreover, these models are characterized as "sloppy" in the sense that the curvature of the manifold is much higher with some directions in

the phase space than the others [49]. This sloppiness character makes it more difficult to fit the potential for large number of parameters.

One of the class of methods used for global optimization of parameters of such nonlinear models is meta-heuristic algorithms in which many methods employ some form of stochasticity. Such methods include Simulated Annealing [50], Genetic algorithms and Particle Swarm Optimization (PSO) [51, 52, 53]. In this study we use PSO to optimize the SW potential given its optimization success in previous studies [48, 54, 47]

PSO is a nature inspired algorithm from the exploitation behaviour of birds which fly in a swarm. Initialization of the algorithm starts by randomly generating the particles in phase space with given bounds and assigning random velocities to these particles. For each particle a cost function C of the form

$$C(\theta) = \sum_{j=1}^{N} w_j \frac{|d_j - a_j|}{d_j} \tag{2.7}$$

is calculated. Here, d_j is the j^{th} characteristic value which the potential is fit for, a_j is calculated value using the Interatomic potential with the set of parameters θ and w_j is the weight assigned to j^{th} characteristic. At each step the cost function for each particle is calculated and updated only if the new cost function is lower than its lowest cost function obtained at a parametric position $\vec{p}_{ipB}$. This is termed as its personal best position. Likewise at each step the lowest cost function out of all the particles and its parametric position $\vec{g}_B$ is also updated. This is termed as global best position. Equipped with these vectors the i^{th} particle's position $\vec{x}_i$ is updated with a velocity vector $\vec{v}_i$ according to the following equations,

$$\vec{x}_i(t+1) = \vec{x}_i(t) + \vec{v}_i(t+1) \tag{2.8}$$

$$\vec{v}_i(t+1) = w\vec{v}_i(t) + r_1c_1(\vec{p}_{iB} - \vec{x}_i(t)) + r_2c_2(\vec{g}_B - \vec{x}_i(t)) \tag{2.9}$$

Here, w, c_1, and c_2 are constants and r_1 and r_2 are uniformly generated random numbers between 0 and 1. The swarm nature of the bird flocks are reflected in the last two terms in equation (2.3) where the general direction of the particle is determined by the region which has positively rewarded the particle from its

personal experience and also from the region which has been positively rewarded by the whole community of particles.

2.3 Thermal Conductivity

Thermal conductivity is the measure of how well a material is able to propagate heat. Thermal conductivity usually refers to the combination of lattice thermal conductivity κ which employs phonons as its carriers and electric thermal conductivity σ carried by electrons. With the help of *ab initio* methods both of the transport coefficients κ and σ can be obtained. Since we do not use the concept of electrons as particles in classical MD we are left with phonons as the only heat carrier and are only able to measure κ using IPs. In this section, methods for calculating thermal conductivity is discussed.

2.3.1 Non-Equilibrium Molecular Dynamics (NEMD)

NEMD method make use of Fourier's Law to calculate thermal conductivity.

$$\vec{J} = -\kappa \vec{\nabla} T \tag{2.10}$$

$\vec{J}$ is the heatflux and $\vec{\nabla} T$ is the temperature gradient. In general κ is a second rank tensor which accounts for anisotropic thermal conductivities. In simulations, two regions of the system are held at different temperatures by fixing a hot reservoir and a cold reservoir which introduces the thermal gradient across the region. The heat added to the hot reservoir must be subtracted from the cold reservoir and the resulting heat flux required to maintain the temperature gradient is calculated.

The reverse simulation is also carried out (see Figure 2.1) where a known amount of heat energy ΔE is added every time-step Δt at one end of the system and the same amount of energy is subtracted from the system at the opposite end. This is achieved by scaling the velocity vectors in the concerned region and effectively serves as the heat flux $\vec{J}$ introduced to the system. Here, the

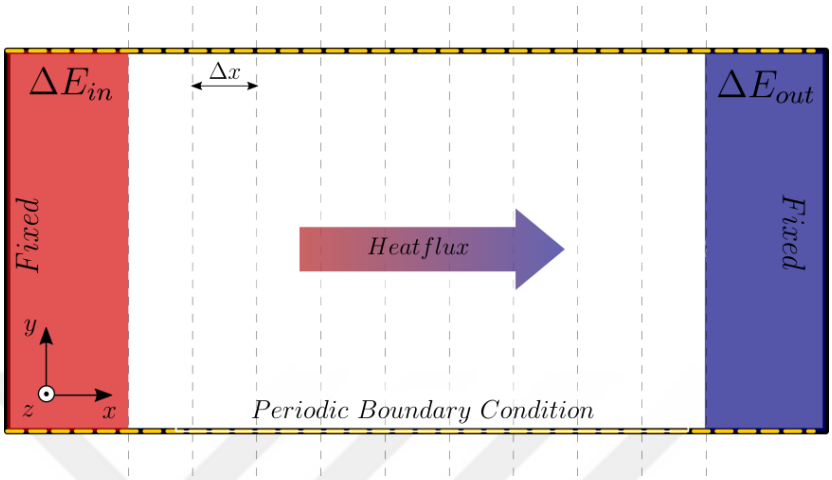

Figure 2.1: Illustration of NEMD simulation method

direction for which κ is calculated has fixed boundary conditions where as the other directions are periodic (For 2D systems the direction perpendicular to the monolayer plane is also fixed). Heat flux is added until the system reaches a steady state and the resulting temperature gradient is calculated. To calculate the temperature gradient, the length of the heatflux direction is divided into chunks of Δx. The kinetic energy of the particles in each chunk is recorded and the corresponding temperature is calculated from the equipartition theorem.

$$E_k = \sum_{i}^{N} \frac{1}{2} m_i v_i^2 = \frac{3}{2} k_B T \tag{2.11}$$

To ensure that the system has reached a steady state, the velocities of the atoms should follow the same Maxwell-Boltzmann distribution as the system prior to the introduction of heat flux.

$$P = 4\pi v^2 \left[\frac{m}{2\pi k_B T}\right]^{\frac{3}{2}} \exp\left(\frac{-mv^2}{2k_B T}\right) \tag{2.12}$$

In the latter scenario κ is calculated as time average of the measured temperature gradient [55]. For the instance shown in Figure 2.1

$$\kappa_{xx} = \lim_{t\to\infty} \frac{\Delta E/\Delta t}{\langle \partial T/\partial x \rangle A_{yz}} \tag{2.13}$$

This direct approach using NEMD is known have a sample size dependent effect on κ since the the system has a fixed boundary condition parallel to the direction

of temperature gradient. To find the infinite length thermal conductivity κ_∞ from finite length L we use the formula [1, 56],

$$\frac{1}{\kappa} = \frac{1}{\kappa_\infty}\left(\frac{l}{L} + 1\right) \tag{2.14}$$

where l is the effective phonon mean free path.

2.3.2 Green-Kubo Method

Green-Kubo method is based on the general Green-Kubo relations [57] which states that

$$\gamma = \int_0^\infty \langle \dot{A}(0) \cdot \dot{A}(t) \rangle dt \tag{2.15}$$

where γ is the transport coefficient and $\dot{A}$ is the time derivative of the related microscopic variable A. It is an equilibrium MD method where the transport coefficient κ tensor is calculated using the heat flux via its integral of equilibrium time correlation function. The equation is given by

$$\kappa_{\alpha\beta} = \frac{V}{k_B T^2} \int_0^\infty \langle J_\alpha(0) J_\beta(t) \rangle dt \tag{2.16}$$

$$J_\alpha(t) = \frac{1}{V}\frac{d}{dt}\left[\sum_i^N E_i r_{i\alpha}\right] = \frac{1}{V}\left[\sum_i^N E_i v_{i\alpha} + \sum_i^N \frac{dE_i}{dt} r_{i\alpha}\right] \tag{2.17}$$

where E_i is the total potential and kinetic energy of atom i and $\alpha, \beta \in \{x, y, z\}$. The first term of the derivative of the macroscopic variable $A = E_i \vec{r}_i$ is the convective term and the other is the virial contribution to the heatflux.

In practice, Green-Kubo method is applied using MD by first placing the system in the canonical ensemble (NVT) at a desired temperature until the system reaches thermal equilibrium. The system is then subject to the microcanonical ensemble (NVE) for statistical time averaging of the heatflux. This is done until the auto-correlation function converges to zero so that integration does not diverge.

2.3.3 Boltzmann Transport Equation (BTE)

BTE describes the behaviour of a non-equilibrium thermodynamic systems. The general form of BTE can be written as

$$\frac{df}{dt} = \left(\frac{df}{dt}\right)_{\text{force}} + \left(\frac{df}{dt}\right)_{\text{diffusion}} + \left(\frac{df}{dt}\right)_{\text{scattering}} \tag{2.18}$$

where f is the distribution function of the concerned system.

A system at equilibrium free from temperature gradients and other external forces is described by the Bose-Einstein distribution $f_0(\omega_\lambda) = 1/(\exp(\frac{\hbar\omega_\lambda}{k_B T}) - 1)$ for phonons. BTE can be used when the system is subject to a temperature gradient $\vec{\nabla}T$ which causes the phonon distribution function f_λ to deviate from f_0. In general this can be denoted as $f_\lambda = f_0 + g_\lambda$. Here $\lambda \equiv (\vec{q}, p)$ refers to the phonon mode at wavevector $\vec{q}$ and branch index p. When the system reaches a steady-state, there is no change in f_λ with respect to time and taking into consideration that external forces do not effect the phonons, BTE takes the form

$$\frac{df_\lambda}{dt} = \left(\frac{df_\lambda}{dt}\right)_{\text{diffusion}} + \left(\frac{df_\lambda}{dt}\right)_{\text{scattering}} = 0 \tag{2.19}$$

The diffusion term can be written as [58]

$$\left(\frac{df_\lambda}{dt}\right)_{\text{diffusion}} = -\vec{\nabla}T \cdot \vec{v}_\lambda \frac{\partial f_\lambda}{\partial T} \qquad \text{where} \quad \vec{v}_\lambda = \frac{\partial \omega}{\partial \vec{q}} \tag{2.20}$$

$\vec{v}_\lambda$ is the phonon group velocity. The scattering term is solved by taking the linear approximation to the deviation of distribution function f_λ with respect to $\vec{\nabla}T$. i.e. by taking $g_\lambda = -\vec{F}_\lambda \cdot \vec{\nabla}T\, df_0/dt$. Further assumptions are taken to simplify BTE by considering two and three phonon scattering processes which results in a linearized BTE formula

$$\vec{F}_\lambda = \tau_\lambda^0 \left(\vec{v}_\lambda + \vec{\Delta}_\lambda\right) \tag{2.21}$$

where τ_λ^0 is the relaxation time of the phonon mode. τ_λ^0 an $\vec{\Delta}_\lambda$ are calculated using second and third order interatomic force constants [59]. $\vec{F}_\lambda$ is used to calculate thermal conductivity by the relation

$$\kappa_{\alpha\beta} = \frac{1}{k_B T^2 V N} \sum_\lambda f_0(f_0 + 1)(\hbar\omega_\lambda)^2 v_\lambda^\alpha F_\lambda^\beta \tag{2.22}$$

Chapter 3

Optimization of Interatomic Potential

3.1 DFT Calculations Details

All of the DFT calculations were conducted using the QUANTUM ESPRESSO code [60]. Optimised norm-conserving Vanderbilt pseudopotentials (ONCVSPC) obtained from PsuedoDojo Project [61] were used to describe the interactions between ionic core and valence electrons. The exchange-correlation potential is treated within the Generalized Gradient Approximated (GGA) modified Perdew-Burke-Ernzerhof (PBEsol) functional. WS_2 lattice structures was optimized by performing a variable cell relaxation until stress components were less than 0.1 kBar. The parameters used for the input script file was obtained using sufficient convergence tests for energy and forces for all the phases of the optimized WS_2 crystal structure. Consistent to the convergence test the wavefunction energy cut-off applied for the calculations were fixed at 950 eV and a Γ centered 24 $\times$ 24 $\times$ 1 Monkhorst-Pack scheme k-point grid was used for the Brillouin zone integration. Since the TMDs used are all monolayer 2D materials, A vacuum of 20Å is used to prevent the periodic image interactions.

Phonon frequencies were obtained using the finite difference method as implemented in Phonopy code [62, 63]. A supercell of 4 x 4 x 1 and a Γ centered k-point grid of 6 x 6 x 1 was used for the finite displacement force calculations for 1H and 1T WS_2 phases. Similarly, for the 1T′ phase a 3 x 3 x 1 supercell and 8 x 8 x 1 k-point grid was used. The phonon dispersion curves along the high symmetry path Γ[0,0,0]-M[1/2,0,0]-K[1/3,1/3,0]-Γ[0,0,0] were obtained for 1H and 1T phase. For the 1T′ phase Γ[0,0,0]- Z[0,1/2,0]-C[1/2,1/2,0]-Y[1/2,0,0]-Γ[0,0,0]) path was taken.

Different types of vacancy defect formation energies (using the notation as described in Karaaslan *et al.* [54]) was also calculated using the formula

$$E_f^{DFT} = E_d - E_p + nE_W + mE_S \tag{3.1}$$

where E_f^{DFT} is the formation energy, E_d is the total energy of the crystal structure with defect, E_p is the total energy of the perfect crystal structure, nE_W is the ground state energy of n number of isolated W atoms and likewise mE_S is the ground state energy of m number of isolated S atoms. Types of vacancy defect structures are illustrated on Figures B.1, B.2, B.3 for 1H, 1T and 1T′ phases respectively.

3.2 Optimization Details

For the optimization of the structures given in Figure 3.1 3.2 3.3, four two-body terms W-W, W-S, $S_{u,d}$-$S_{u,d}$ and S_u-S_d and three three-body terms W-$S_{u,d}$-$S_{u,d}$, $S_{u,d}$-W-W and W-S_u-S_d were considered. Here, the upper layer Sulfur atoms (denoted by subscript u) and bottom layer Sulfur atoms (denoted by subscript d) are distinguished in order to allow flexibility for the IP to describe different interactions within the same sulfur layer and across the Tungsten layer. This is also to distinguish between the three-body bond bending terms.

Optimization was carried out for the modified SW potential parameters σ, A, B, θ_0, r^{max}, λ and γ. Since r^{max} is considered as the cutoff distance it is

predetermined to the optimization as the midway length between the first and second nearest neighbours of the respective bond type. Likewise the θ_0 is chosen as the DFT optimized rest angle of the 1H phase. To further reduce the amount of parameters, B is constrained as a function of σ, r^{max}, and DFT calculated rest bond length d of the 1H phase.

$$B = \frac{d^5}{\sigma^4 d + 4\sigma^3 (d - r^{max})^2} \tag{3.2}$$

As for the threebody cutoff parameters δ_1 and δ_2 was chosen as 0.25 and 0.35.

PSO algorithm was implemented to optimize a total set of 13 parameters. For cost function C the target characteristics chosen were, the cohesive energy, lattice constants, TMD layer thickness, vacancy formation energies and the phonon frequencies. The calculated characteristic values using DFT and optimized SW potential are given in Tables 3.1, 3.2, 3.3 for 1H, 1T, and 1T′ phases respectively.

The main weight in the cost function was assigned to the acoustic phonon frequencies to properly reproduce the vibrational properties of the material. In order to fit the SW potential for the negative frequency modes of 1T phase, θ_0 for W-S_u-S_d was chosen as 165.3706 which is one of the rest bond angle for the 1T′ phase.

The optimized parameters in LAMMPS format are given in Tables 3.4 3.5, 3.6 3.7 and 3.8 3.9 for 1H, 1T and 1T′ phases respectively.

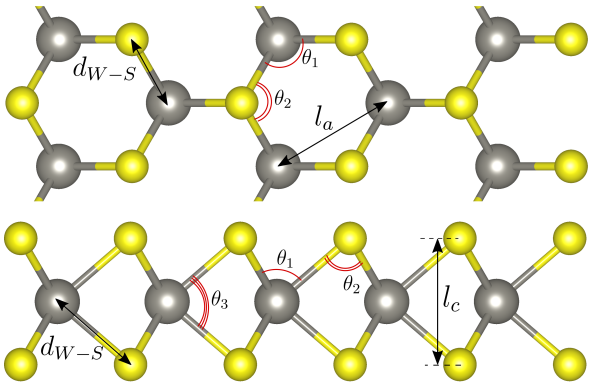

Figure 3.1: Top and cross-sectional view 1H-WS_2 crystal structure.

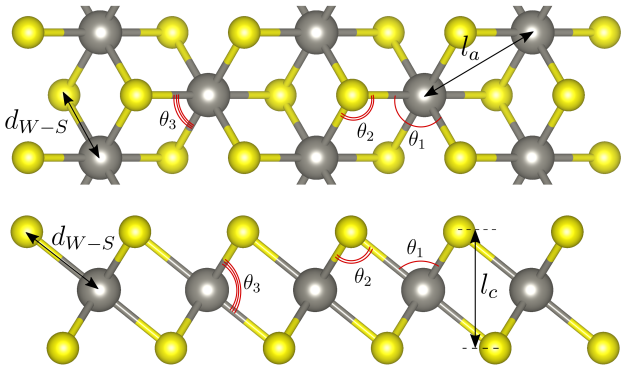

Figure 3.2: Top and cross-sectional view 1T-WS_2 crystal structure.

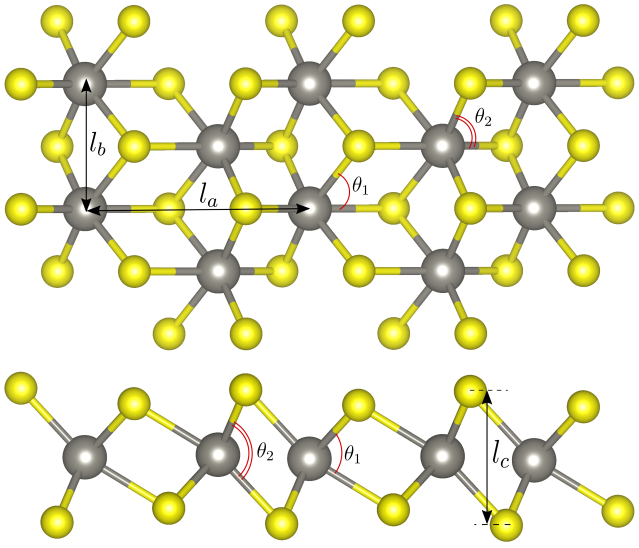

Figure 3.3: Top and cross-sectional view 1T′-WS_2 crystal structure.

	E_{cohesive}	l_a	l_c	d_{W-S}	θ_1	θ_2	θ_3	V_S
DFT	-5.300	3.1594	3.1395	2.4065	82.0551	82.0551	81.4287	4.9571
SW	-4.1842	3.1594	3.1395	2.4065	82.0551	82.0551	81.4288	5.4237
	V_{2S}	V_{W+2S}	V_{W+S}	V_W	V_{3W+2S}	V_{W+3S}	V_{W+6S}	
DFT	10.2638	21.9450	17.2507	13.1266	42.0070	25.6497	39.8601	
SW	10.8383	22.1613	18.2140	14.2576	42.0804	25.6206	36.9560	

Table 3.1: Comparison of Structural and Vacancy defect properties obtained using DFT and the optimized SW potential for 1H-WS_2. Energies are given in eV and lengths in Å

	E_{cohesive}	l_a	l_c	d_{W-S}	θ_1	θ_2	θ_3	V_S
DFT	-5.1520	3.1927	3.1460	2.4232	82.4127	82.4127	97.5873	4.4749
SW	-3.9979	3.1983	2.9705	2.3697	84.8801	84.8801	95.1199	6.2992
	V_{2S}	V_{W+2S}	V_{W+S}	V_W	V_{3W+S}	V_{3W+4S}	V_{W+3S}	V_{W+6S}
DFT	9.0809	20.0504	15.8265	11.6888	38.1342	46.7895	24.0098	36.9884
SW	12.5026	20.0273	15.6460	11.1688	34.3315	41.7364	24.3276	36.9116

Table 3.2: Comparison of Structural and Vacancy defect properties obtained using DFT and the optimized SW potential for 1T-WS_2. Energies are given in eV and lengths in Å

	E_{cohesive}	l_a	l_b	l_c	θ_1	θ_2	V_S
DFT	-5.1520	5.7234	3.1862	3.4055	81.4290	107.7753	4.7073
SW	-1.9827	5.8441	3.2534	2.6991	86.2532	89.2452	4.9476
	$V_{S(2)}$	V_{2S}	$V_{2S(2)}$	$V_{2S(3)}$	V_W	V_{W+S}	$V_{W+S(2)}$
DFT	5.1653	9.6716	10.3094	9.9524	12.4897	16.3478	16.3599
SW	4.9280	9.7856	9.8419	8.5794	1.9798	6.9077	6.9273

Table 3.3: Comparison of Structural and Vacancy defect properties obtained using DFT and the optimized SW potential for 1T′-WS_2. Energies are given in eV and lengths in Å

	σ	A	B	r^{min}	r^{max}
$S_{u,d}$-$S_{u,d}$	2.0217	2.2124	3.2867	0.00	4.30
$S_{u,d}$-$S_{d,u}$	2.0463	0.3142	3.7916	0.00	4.00
W-$S_{u,d}$	1.4499	9.5574	3.2016	0.00	3.50
W-W	0.6840	2.3432	133.5876	0.00	4.30

Table 3.4: 1H-WS_2 Two-Body Stillinger Weber parameters in LAMMPS format

	λ	γ_{12}	γ_{13}	θ_0	r_{12}^{max}	r_{13}^{max}
W-$S_{u,d}$-$S_{u,d}$	146.6788	1.9476	1.9476	82.0551	3.50	3.50
$S_{u,d}$-W-W	69.7034	1.8717	1.8717	82.0551	3.50	3.50
W-S_u-S_d	106.1704	1.9476	1.9476	81.4287	3.50	3.50

Table 3.5: 1H-WS_2 Three-Body Stillinger Weber parameters in LAMMPS format

	σ	A	B	r^{min}	r^{max}
$S_{u,d}$-$S_{u,d}$	2.9994	3.5903	0.7946	0.00	4.30
$S_{u,d}$-$S_{d,u}$	1.3551	2.3041	16.9812	0.00	4.00
W-$S_{u,d}$	0.9676	6.8470	12.5263	0.00	3.50
W-W	2.9632	0.1065	0.8305	0.00	4.30

Table 3.6: 1T-WS_2 Two-Body Stillinger Weber parameters in LAMMPS format

	λ	γ_{12}	γ_{13}	θ_0	r_{12}^{max}	r_{13}^{max}
W-$S_{u,d}$-$S_{u,d}$	97.3306	2.0665	2.0665	82.0551	3.50	3.50
$S_{u,d}$-W-W	1.0540	1.8333	1.8333	82.0551	3.50	3.50
W-S_u-S_d	1955.3595	2.0665	2.0665	164.0177	3.50	3.50

Table 3.7: 1T-WS_2 Three-Body Stillinger Weber parameters in LAMMPS format

	σ	A	B	r^{min}	r^{max}
$S_{u,d}$-$S_{u,d}$	2.6138	2.3872	1.3094	0.00	4.30
$S_{u,d}$-$S_{d,u}$	0.2983	2.4690	2943.7239	0.00	4.00
W-$S_{u,d}$	3.3893	13.2333	0.1602	0.00	3.50
W-W	1.8277	1.5639	4.6958	0.00	4.30

Table 3.8: 1T′-WS_2 Two-Body Stillinger Weber parameters in LAMMPS format

	λ	γ_{12}	γ_{13}	θ_0	r_{12}^{max}	r_{13}^{max}
W-$S_{u,d}$-$S_{u,d}$	1.7601	0.3482	0.3482	82.0551	3.50	3.50
$S_{u,d}$-W-W	25.5766	0.8815	0.8815	82.0551	3.50	3.50
W-S_u-S_d	419.9901	0.3482	0.3482	164.0177	3.50	3.50

Table 3.9: 1T′-WS_2 Three-Body Stillinger Weber parameters in LAMMPS format

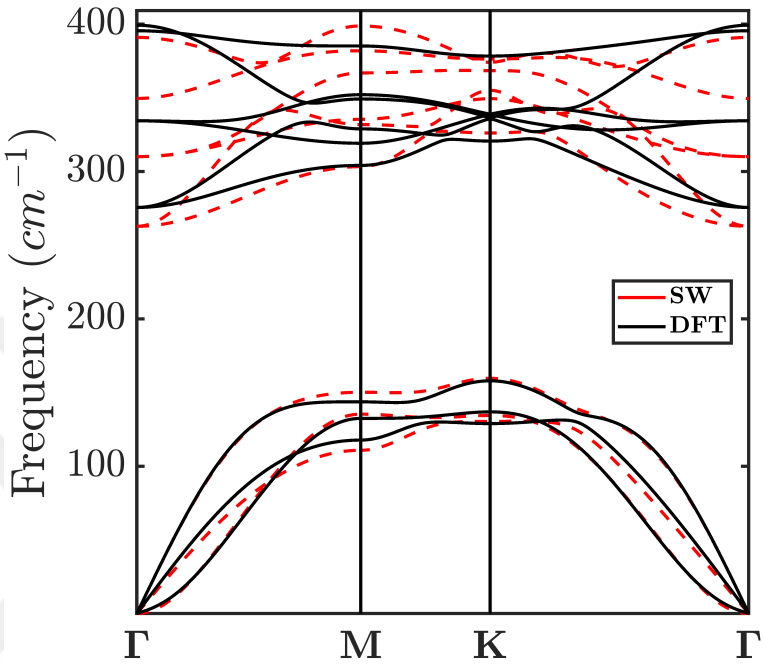

Figure 3.4: 1H-WS_2 Phonon Band-Structure along high-symmetry path.

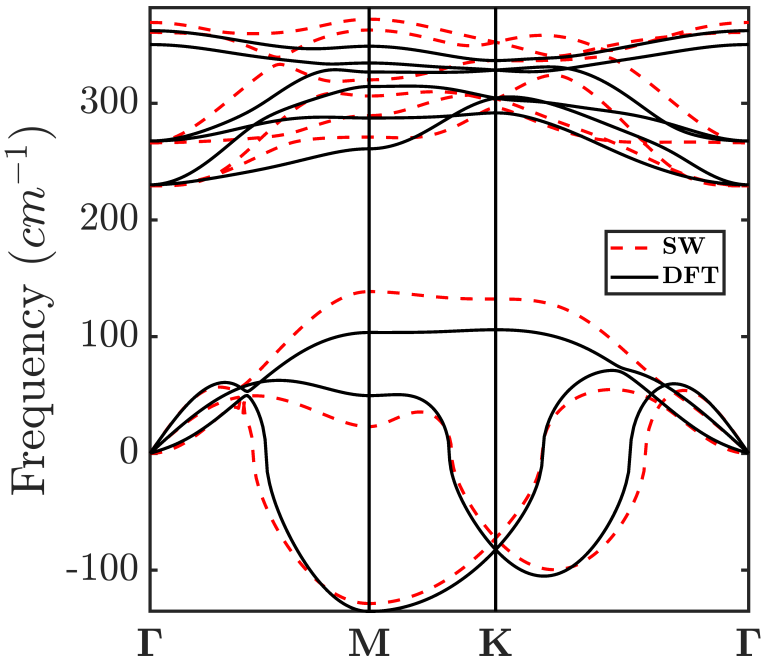

Figure 3.5: 1T-WS_2 Phonon Band-Structure along high-symmetry path.

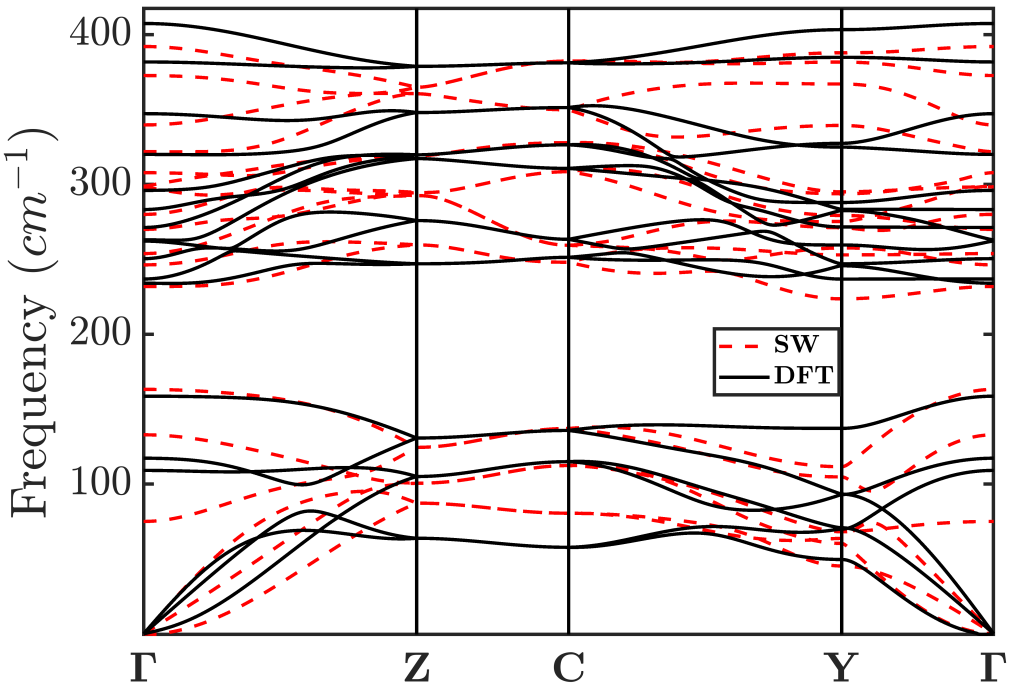

Figure 3.6: 1T′-WS_2 Phonon Band-Structure along high-symmetry path.

Chapter 4

Thermal Conductivity Assessment

4.1 BTE solution using DFT

Under quantum mechanical treatment, lattice thermal conductivity of the three WS_2 phases were computed by solving the BTE. ShengBTE [59] and thirdorder.py [64] codes were used to calculate the thermal conductivity. In order to calculate the third-order force constants, finite displacements files were generated using thirdorder.py. For the 1H(1T) phase 188(176) such displacement files were generated using a 3 x 3 x 1 supercell. Likewise for the 1T′ phase 300 displacement files were generated using a 2 x 2 x 1 supercell. In all of the cases interactions up to 3rd nearest neighbour was considered. The forces resulting from the finite displacements were calculated using QUANTUM ESPRESSO with the same settings previously used for second order force constants. However here we use a Γ centered k-point grid of 8 x 8 x 1. Third-order force constants were calculated from the resulting force files using thirdorder.py and both second-order and third-order force constant files were fed into ShengBTE to calculate thermal conductivity. The results obtained are given in Figure 4.1. For the 1H phase high thermal conductivity is expected relative to the 1T and 1T′ phases. Lowest

thermal conductivities are predicted in 1T phase. Anisotropy of thermal conductivity is also expected for 1T′ due to its structural asymmetry. All thermal conductivities decrease with increasing temperature.

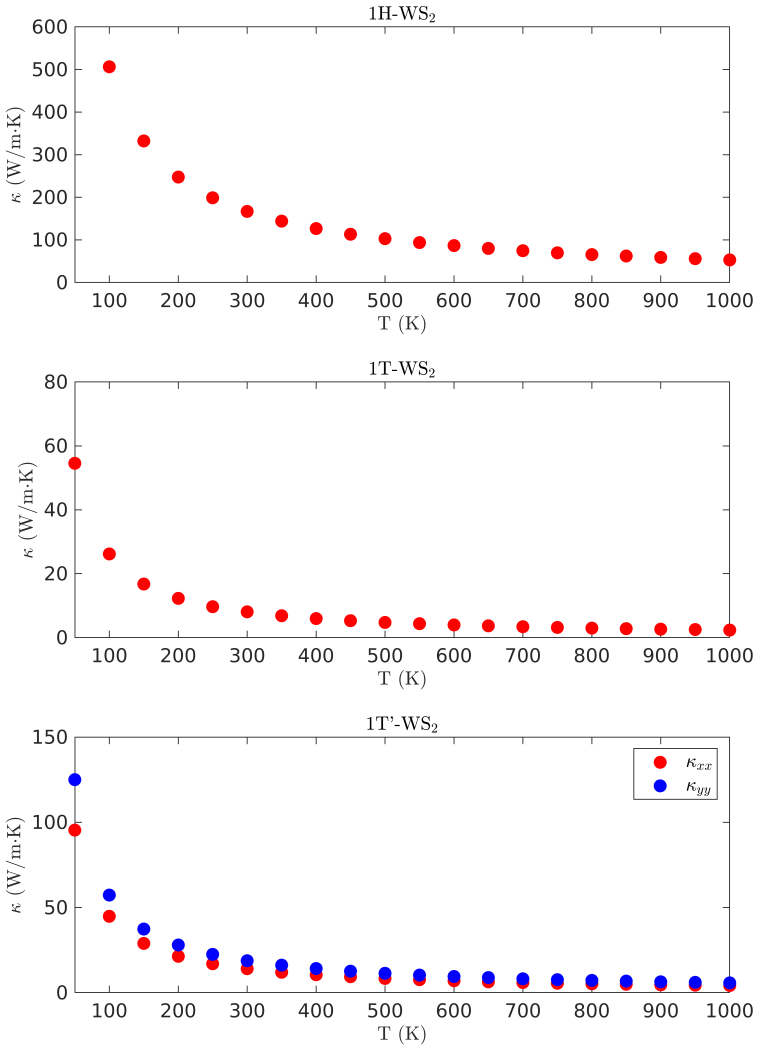

Figure 4.1: Thermal Conductivity Calculated using BTE for 1H, 1T and 1T′ phases of WS_2

4.2 NEMD Computational details and Results

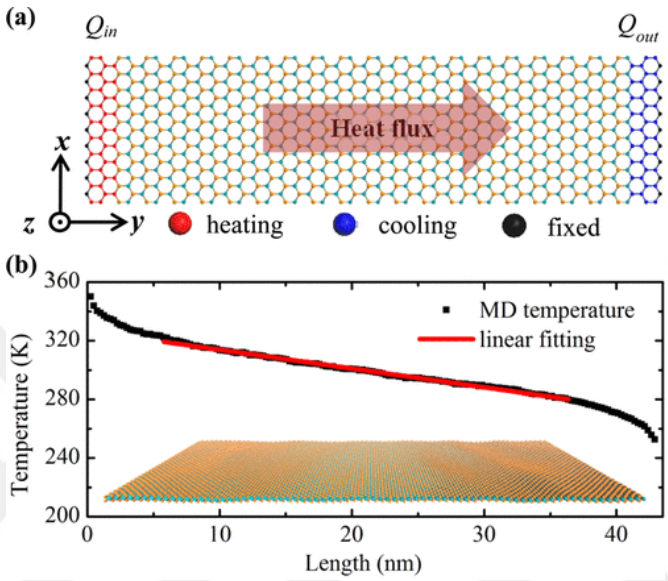

Figure 4.2: (a) Illustration of NEMD method applied for monolayer WS_2. Outermost atoms in the y direction are held in place while the next two blocks of atoms are designated as the heating and cooling regions. (b) Thermal gradient formed in the heatflux region. The ends of the black line show non-linear behaviour at the heating and cooling regions. Reprinted with permission from The Journal of Physical Chemistry C (Reference [1]). Copyright 2016 American Chemical Society

All MD simulations were carried out using LAMMPS [65]. The NEMD method was applied to finite-length WS_2 nanoribbons. Periodic boundary conditions are only applied in the width directions whereas the other boundaries are fixed. The trajectory of the system was integrated using a timestep of 0.5 fs. The nanoribbion is first placed in the canonical ensemble (NVT) at a temperature of 300K for 100 ps and then in the microcanonical ensemble (NVE) for another 100 ps. After this, the NEMD method is applied until the system reaches a steady-state. The simulation is run for a total of 600 ps. Time average of the kinetic energies of the heatflux region chunks are obtained in the last 100 ps. These kinetic energies are converted to temperature using formula (2.11) and the temperature gradient is calculated using linear interpolation. A typical interpolation of the gradient formed is given in Figure 4.3. The data points in the non-linear regime is omitted during interpolation due to the non-equilibrium features as a result of

fast energy exchange and rapid phonon boundary scatterings at the fixed ends of the nanoribbons [1]. The thermal conductivity is then calculated using the gradient as discussed in Chapter 2.

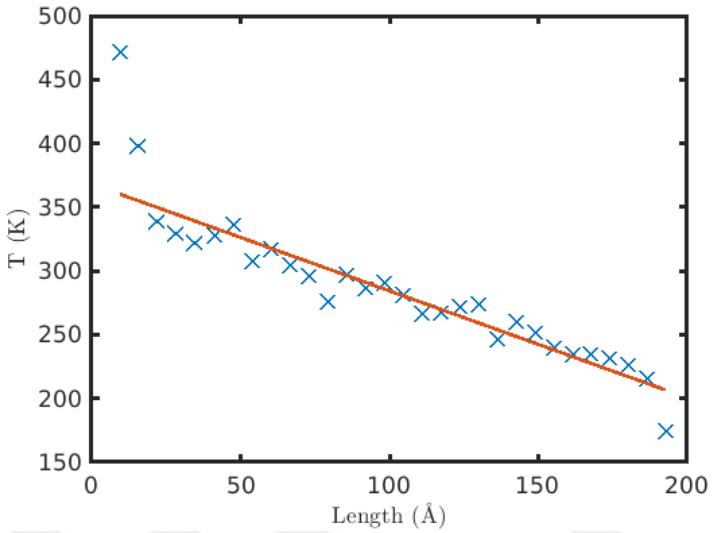

Figure 4.3: Typical linear interpolation for temperature gradient calculations

4.2.1 1H-WS_2 Results and Discussion

To investigate the effect of size on thermal conductivity κ, 4 different nanoribbon samples of length 10.11, 19.90, 40.12, and 79.93 nm were prepared. The width of the samples were fixed at 10.4 nm. A heat flux of $J = 9.613 \times 10^{-7}$ W/m^2 was added and removed from the sample simultaneously from the heating and cooling regions respectively. To obtain accurate results, 10 independent simulations were carried out per sample each with a different initial velocity seed. The results are then averaged out to calculate the thermal conductivity. The results obtained are given in Figure 4.4 (left). The calculated κ values increases monotonically from 18.69 to 70.63 W with the increase in sample size from 10.11 to 79.93 nm. To predict the infinite-length κ value, a graph of $1/\kappa$ vs 1/Length was plotted and linearly interpolated (Figure 4.4 right) to use formula (2.14). With the given 4 data points, the infinite length sample has an estimated κ value of 138.98 W/(m·K). This is in relatively good agreement with the theoretical prediction

(166.75 W/(m·K) at 300K) obtained using BTE.

To examine the effect of temperature on κ, 80 nm samples of 1H-WS_2 is placed in NVT ensemble of temperatures 100, 200, 300, 400 and 500 K at the start of the simulation. (See Figure 4.5). The results obtained shows monotonically decreasing thermal conductivity with increasing temperature. κ values decrease from 111 to 60 W/(m·K) as temperature is increased from 100 to 500K. This is an overall decrease of 46% in thermal conductivity from 100 to 500K.

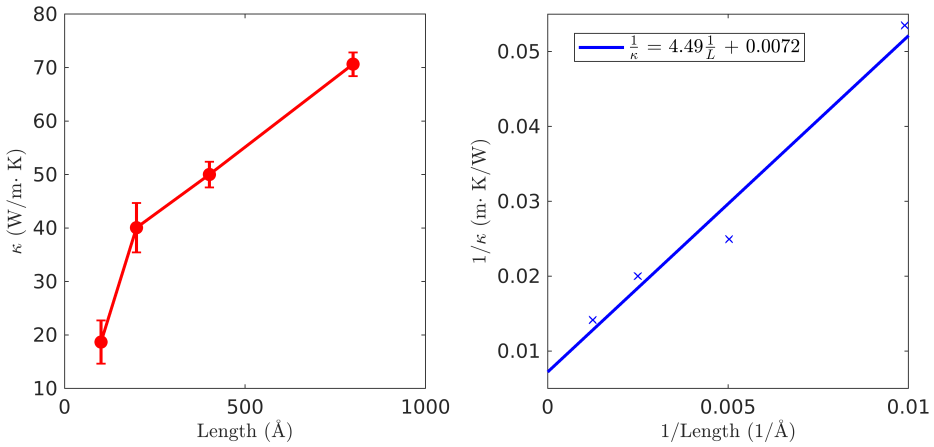

Figure 4.4: (left) 1H-WS_2 κ values of finite length nanoribbons. Error bars show standard deviation. (right) Linear plot to calculate infinite length κ value.

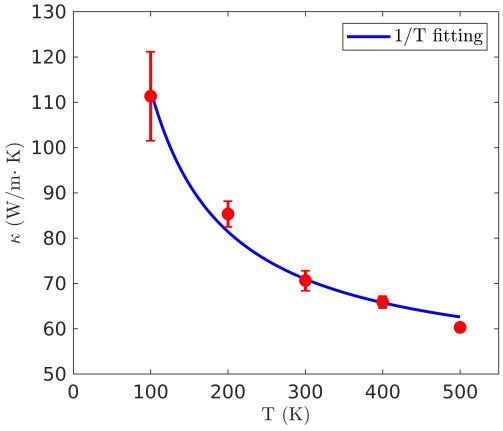

Figure 4.5: Thermal conductivity κ as a function of Temperature calculated using 1H-WS_2 nanoribbon of length ∼80 nm

4.2.2 1T′-WS_2 Results and Discussion

Similar to the 1H phase, NEMD method was applied to 1T′ phase with nanoribbons elongated in the x direction (l_a lattice constant direction in Figure 3.3) with lengths of 10.51, 19.87, 39.74, 80.06 nm where the width was fixed at 10.08 nm. In addition to this, another set of samples where the nanoribbons elongated in y direction (l_b lattice constant direction in Figure 3.3) with lengths 9.87, 20.07, 40.14, 79.97 nm were prepared. Here the width of the sample in the x direction was fixed at 10.3 nm. In both cases a heat flux of $J = 1.06 \times 10^{-8}$ W/m^2 was supplied and the simulation was carried out at 50K due to higher temperature instabilities of the structure. The obtained results for x and y direction are given in Figure 4.6. In the x-direction, finite length κ_x values increase monotonically from 3.68 to 26.7 W/(m·K) as nanoribbion length is increased from ∼10 to 80 nm. In the y-direction, similar trend is observed from 4.15 to 31.1 W/(m·K) as nanoribbion length is increased from ∼10 to 80 nm.

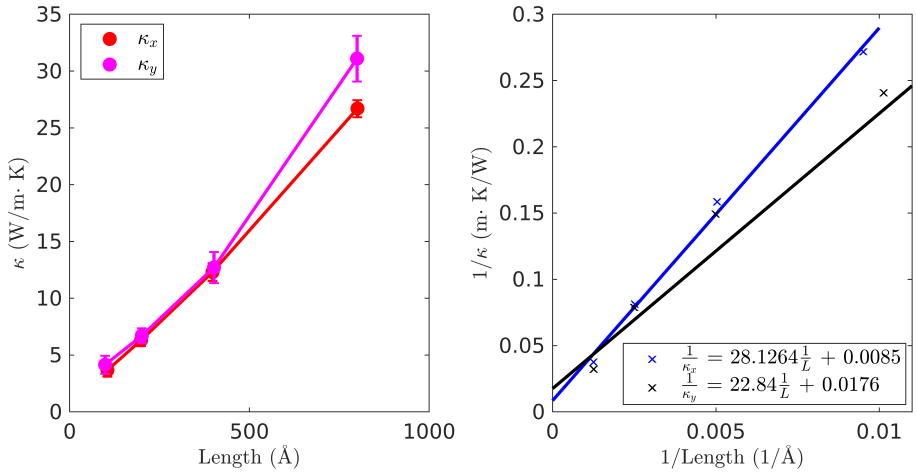

Figure 4.6: (left) 1T′-WS_2 κ values of finite length nanoribbons. Error bars show standard deviation. (right) Linear plot to calculate infinite length κ value.

Using interpolation, the estimated value of infinite length κ_x and κ_y values were calculated as 117 and 56 W/(m·K) respectively. The system shows anisotropic behaviour of thermal conductivity, although only κ_x value match closely with the theoretically predicted value of 95 W/(m·K). Interpolation of κ_y values suggest a lower thermal conductivity because of the deviation of ∼ 10nm ribbon data point.

The finite length κ values also shows that while at shorter lengths the deviation in κ_x and κ_y is minimal, at longer lengths there is significant deviation in thermal conductivity suggesting that the anisotropy in the perpendicular directions is caused by phonons with longer mean free paths.

4.2.3 1T-WS_2 Results nd Discussion

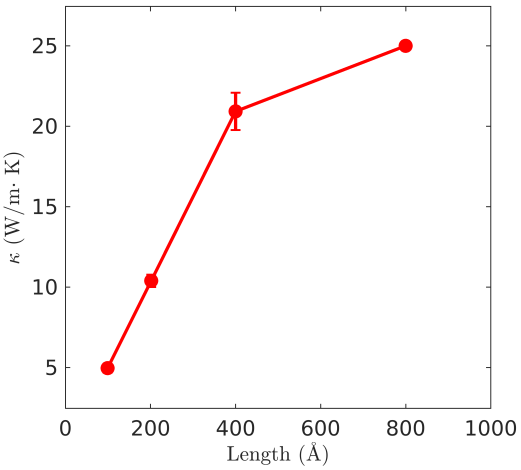

Figure 4.7: 1T-WS_2 κ values of finite length nanoribbons. Error bars show standard deviation.

NEMD method was applied to 1T phase with nanoribbons of lengths 9.91, 20.14, 39.97, 79.95 nm with a fixed width of 10.52 nm. For the given results in Figure 4.7, simulations were carried out at a temperature of 100K and a heat flux of $J = 1.06 \times 10^{-7}$ W/m^2. The finite length κ value increases monotonically from 4.96 to 25 W/(m·K) as the length is increased from 9.91 to 79.95 nm. The results obtained using ∼80nm ribbons indicate that the 1T phase at 100K has significantly lower thermal conductivity (25 W/(m·K)) compared to that of 1H phase (111.35 W/(m·K)) which is also suggested by the BTE theoretical predictions.

In Fig 4.7, the data points acquired for specific lengths is the average κ of varying number of simulations (with different initial velocity seed). For each length a total 20 nemd simulations were carried out, out of which most of the

simulations resulted in huge temperature drifts under microcanonical ensemble (NVE) and heat-flux, indicating higher kinetic energy in the system. Specifically, for lengths of 9.91, 20.14, 39.97, 79.95 nm the number of viable NEMD simulations obtained (out of 20) were 7, 3, 3 and 1 respectively. The simulations were also repeated under low temperature conditions and various heat flux parameters in which similar results were found.

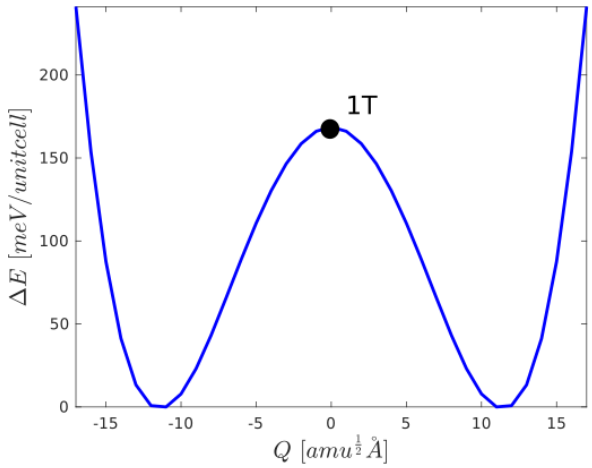

Figure 4.8: Change of energy in the system ΔE as a result of atomic position modulation according to M symmetry point eigenvectors of 1T-WS_2 negative phonon branch obtained using SW potential. Here Q is the displacement amplitude as given in equation A.1

This observation could be attributed to the dynamic instability of 1T structure suggested by the imaginary phonon modes (Figure 3.5). The imaginary phonon modes are caused by negative second order force constants as a result of concavity in some region of the PES. Using the eigenvectors of the phonon modes, atomic positions of the crystal structure can be modulated to observe this concavity in total energy of the system (see Figure 4.8). For the 1T structure the system is held in an unstable fixed point. Under NVT conditions (where energy of the system is allowed to fluctuate), regions of the system may fluctuate around the unstable point while other parts of the system displacively transit into the lower energy minimum causing a slight change in the total energy while maintaining the total kinetic energy of the system. This picture is substantiated with one of the simulations carried out with a $\sim$ 10x10 nm sample (See Figure 4.9,4.10)

whereby the displacive phase transition had occurred in the sample.

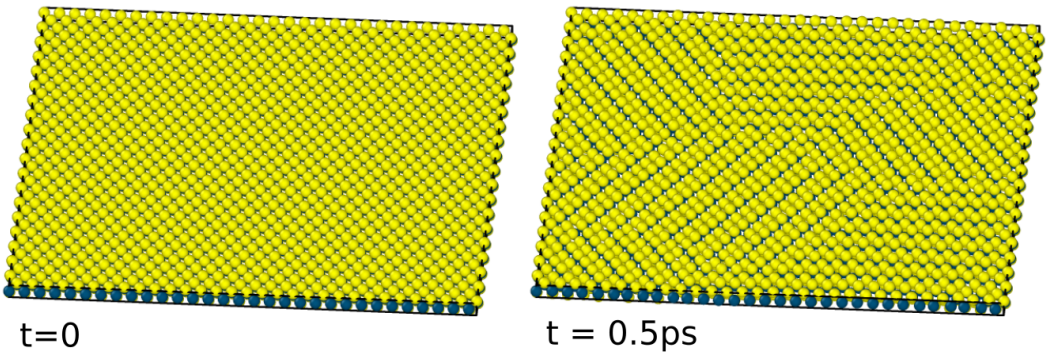

Figure 4.9: (left) Atomic positions showing perfect 1T crystal structure at the start of simulation. (right) Buckled structure formation after 0.5ps. Rendering of the crystal structure was carried out using OVITO [2] package

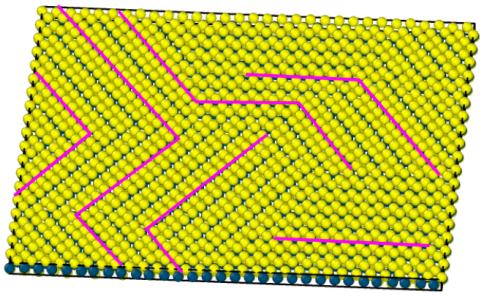

Figure 4.10: Tracing of buckled structures along its formation directions

Figure 4.9 and 4.10 shows that the 1T sample had formed buckled structures along the three-fold rotationally symmetric directions of the 1T-WS_2. Under NVE conditions the buckled structure randomly formed in the symmetrical directions are unstable at the fixed edges of the heatflux direction causing the system to disintegrate which results in the temperature drift.

Chapter 5

Conclusion

In conclusion, we optimized three separate parameter sets for Stillinger-Weber potential to model the structure and certain characteristics of 1H, 1T and 1T′ phases of WS_2 using particle-swarm optimization. The characteristics obtained using optimized SW potential for 1H phase are in good agreement with the results obtained using DFT. For the metallic 1T and 1T′ phases, some of the characteristics deviates slightly from the expected values. We also note that for the metallic phases there is a high three-body contribution to the interatomic potential arising from W-S_u-S_d bond bending term. In contrast to semiconducting 1H phase, these three-body contributions in the mettalic phase is almost comparable to the two-body contributions which makes the optimization for these phases a significant challenge.

Equipped with these potentials, we assess their accuracy in describing the thermal conductivity of each phase using NEMD method. 1H NEMD results show 300K thermal conductivity in close agreement with first principle κ predictions obtained using BTE. Finite-length 1H nanoribbon samples was also shown to exhibit thermal conductivity which decreases inversely with temperature. 1T′ NEMD simulations were carried out at a lower temperature of 50K where both κ_x and κ_y showed lower thermal conductivity compared with that of 1H phase which is expected from BTE predictions. 1T′ was also shown to exhibit anisotropic

thermal conductivities with longer length nanoribbons. 1T NEMD results show good general trends in thermal conductivity with increase in nanoribbon length. The results obtained using 1T are inconclusive due to its dynamic instability with buckled structure formation along symmetric directions of the 1T structure.

Bibliography

[1] Y. Hong, J. Zhang, and X. C. Zeng, "Thermal conductivity of monolayer mose2 and mos2," *The Journal of Physical Chemistry C*, vol. 120, no. 45, pp. 26067–26075, 2016.

[2] A. Stukowski, "Visualization and analysis of atomistic simulation data with ovito–the open visualization tool," *Modelling and Simulation in Materials Science and Engineering*, vol. 18, p. 015012, dec 2009.

[3] K. S. Novoselov, A. K. Geim, S. V. Morozov, D. Jiang, Y. Zhang, S. V. Dubonos, I. V. Grigorieva, and A. A. Firsov, "Electric field effect in atomically thin carbon films," *Science*, vol. 306, no. 5696, pp. 666–669, 2004.

[4] K. S. Novoselov, D. Jiang, F. Schedin, T. J. Booth, V. V. Khotkevich, S. V. Morozov, and A. K. Geim, "Two-dimensional atomic crystals," *Proceedings of the National Academy of Sciences*, vol. 102, no. 30, pp. 10451–10453, 2005.

[5] Q. H. Wang, K. Kalantar-Zadeh, A. Kis, J. N. Coleman, and M. S. Strano, "Electronics and optoelectronics of two-dimensional transition metal dichalcogenides," *Nature Nanotechnology*, vol. 7, pp. 699–712, Nov 2012.

[6] B. Radisavljevic, A. Radenovic, J. Brivio, V. Giacometti, and A. Kis, "Single-layer mos2 transistors," *Nature Nanotechnology*, vol. 6, pp. 147–150, Mar 2011.

[7] Y. Yoon, K. Ganapathi, and S. Salahuddin, "How good can monolayer mos2 transistors be?," *Nano Letters*, vol. 11, no. 9, pp. 3768–3773, 2011. PMID: 21790188.

[8] O. Lopez-Sanchez, D. Lembke, M. Kayci, A. Radenovic, and A. Kis, "Ultrasensitive photodetectors based on monolayer mos2," *Nature Nanotechnology*, vol. 8, pp. 497–501, Jul 2013.

[9] A. Carladous, R. Coratger, F. Ajustron, G. Seine, R. Péchou, and J. Beauvillain, "Light emission from spectral analysis of Au/mos_2 nanocontacts stimulated by scanning tunneling microscopy," *Phys. Rev. B*, vol. 66, p. 045401, Jun 2002.

[10] A. Splendiani, L. Sun, Y. Zhang, T. Li, J. Kim, C.-Y. Chim, G. Galli, and F. Wang, "Emerging photoluminescence in monolayer mos2," *Nano Letters*, vol. 10, no. 4, pp. 1271–1275, 2010. PMID: 20229981.

[11] G. Eda, H. Yamaguchi, D. Voiry, T. Fujita, M. Chen, and M. Chhowalla, "Photoluminescence from chemically exfoliated mos2," *Nano Letters*, vol. 11, no. 12, pp. 5111–5116, 2011. PMID: 22035145.

[12] M. Acerce, D. Voiry, and M. Chhowalla, "Metallic 1t phase mos2 nanosheets as supercapacitor electrode materials," *Nature Nanotechnology*, vol. 10, pp. 313–318, Apr 2015.

[13] J. Lu, G. Xia, S. Gong, C. Wang, P. Jiang, Z. Lin, D. Wang, Y. Yang, and Q. Chen, "Metallic 1t phase mos2 nanosheets decorated hollow cobalt sulfide polyhedra for high-performance lithium storage," *J. Mater. Chem. A*, vol. 6, pp. 12613–12622, 2018.

[14] X. Geng, Y. Jiao, Y. Han, A. Mukhopadhyay, L. Yang, and H. Zhu, "Freestanding metallic 1t mos2 with dual ion diffusion paths as high rate anode for sodium-ion batteries," *Advanced Functional Materials*, vol. 27, no. 40, p. 1702998, 2017.

[15] Y. Ge, W. Wan, Y. Ren, and Y. Liu, "Large thermoelectric power factor of high-mobility transition-metal dichalcogenides with $1T''$ phase," *Phys. Rev. Res.*, vol. 2, p. 013134, Feb 2020.

[16] M. L. Pereira Júnior, C. M. Viana de Araújo, J. M. De Sousa, R. T. de Sousa Júnior, L. F. Roncaratti Júnior, W. Ferreira Giozza, and L. A.

Ribeiro Júnior, "On the elastic properties and fracture patterns of mox2 (x = s, se, te) membranes: A reactive molecular dynamics study," *Condensed Matter*, vol. 5, no. 4, 2020.

[17] T. S. Akash, R. A. S. I. Subad, P. Bose, and M. M. Islam, "Atomic scale insights into the mechanical characteristics of monolayer 1t-titanium disulphide: A molecular dynamics study," 2020.

[18] M. Maździarz, "Transferability of molecular potentials for 2d molybdenum disulphide," *Materials*, vol. 14, no. 3, 2021.

[19] F. H. Stillinger and T. A. Weber, "Computer simulation of local order in condensed phases of silicon," *Phys. Rev. B*, vol. 31, pp. 5262–5271, Apr 1985.

[20] Y. Mishin, "Machine-learning interatomic potentials for materials science," *Acta Materialia*, vol. 214, p. 116980, 2021.

[21] J. Tersoff, "New empirical approach for the structure and energy of covalent systems," *Physical Review B*, vol. 37, no. 12, p. 6991 – 7000, 1988. Cited by: 2993.

[22] J. Tersoff, "Empirical interatomic potential for silicon with improved elastic properties," *Physical Review B*, vol. 38, no. 14, p. 9902 – 9905, 1988. Cited by: 1436.

[23] J. Tersoff, "Modeling solid-state chemistry: Interatomic potentials for multicomponent systems," *Physical Review B*, vol. 39, no. 8, p. 5566 – 5568, 1989. Cited by: 3843.

[24] D. W. Brenner, O. A. Shenderova, J. A. Harrison, S. J. Stuart, B. Ni, and S. B. Sinnott, "A second-generation reactive empirical bond order (rebo) potential energy expression for hydrocarbons," *Journal of Physics: Condensed Matter*, vol. 14, p. 783, jan 2002.

[25] M. S. Daw and M. Baskes, "Semiempirical, quantum mechanical calculation of hydrogen embrittlement in metals," *Physical Review Letters*, vol. 50, no. 17, p. 1285 – 1288, 1983. Cited by: 2466.

[26] M. S. Daw and M. Baskes, "Embedded-atom method: Derivation and application to impurities, surfaces, and other defects in metals," *Physical Review B*, vol. 29, no. 12, p. 6443 – 6453, 1984. Cited by: 6236.

[27] J. Behler and M. Parrinello, "Generalized neural-network representation of high-dimensional potential-energy surfaces," *Phys. Rev. Lett.*, vol. 98, p. 146401, Apr 2007.

[28] V. Botu, R. Batra, J. Chapman, and R. Ramprasad, "Machine learning force fields: Construction, validation, and outlook," *The Journal of Physical Chemistry C*, vol. 121, no. 1, pp. 511–522, 2017.

[29] M. Novotni and R. Klein, "Shape retrieval using 3d zernike descriptors," *Computer-Aided Design*, vol. 36, no. 11, pp. 1047–1062, 2004. Solid Modeling Theory and Applications.

[30] A. V. Shapeev, "Moment tensor potentials: A class of systematically improvable interatomic potentials," *Multiscale Modeling & Simulation*, vol. 14, no. 3, pp. 1153–1173, 2016.

[31] A. P. Bartók, R. Kondor, and G. Csányi, "Publisher's note: On representing chemical environments [phys. rev. b 87, 184115 (2013)]," *Phys. Rev. B*, vol. 87, p. 219902, Jun 2013.

[32] A. Thompson, L. Swiler, C. Trott, S. Foiles, and G. Tucker, "Spectral neighbor analysis method for automated generation of quantum-accurate interatomic potentials," *Journal of Computational Physics*, vol. 285, pp. 316–330, 2015.

[33] C. Chen and S. P. Ong, "A universal graph deep learning interatomic potential for the periodic table," *Nature Computational Science*, vol. 2, pp. 718–728, Nov 2022.

[34] A. P. Bartók, M. C. Payne, R. Kondor, and G. Csányi, "Gaussian approximation potentials: The accuracy of quantum mechanics, without the electrons," *Phys. Rev. Lett.*, vol. 104, p. 136403, Apr 2010.

[35] T. Mueller, A. G. Kusne, and R. Ramprasad, *Machine Learning in Materials Science*, ch. 4, pp. 186–273. John Wiley Sons, Ltd, 2016.

[36] J.-W. Jiang, "Misfit strain-induced buckling for transition-metal dichalcogenide lateral heterostructures: A molecular dynamics study," *Acta Mechanica Solida Sinica*, vol. 32, no. 1, p. 17–28, 2018.

[37] Z. Jian, Z. Kaiming, and X. Xide, "Modification of stillinger-weber potentials for si and ge," *Phys. Rev. B*, vol. 41, pp. 12915–12918, Jun 1990.

[38] X. W. Zhou, D. K. Ward, J. E. Martin, F. B. van Swol, J. L. Cruz-Campa, and D. Zubia, "Stillinger-weber potential for the ii-vi elements zn-cd-hg-s-se-te," *Phys. Rev. B*, vol. 88, p. 085309, Aug 2013.

[39] M. Ichimura, "Stillinger-weber potentials for iii–v compound semiconductors and their application to the critical thickness calculation for inas/gaas," *physica status solidi (a)*, vol. 153, no. 2, pp. 431–437, 1996.

[40] A. S. Barnard and S. P. Russo, "Development of an improved stillinger-weber potential for tetrahedral carbon using ab initio (hartree-fock and mp2) methods," *Molecular Physics*, vol. 100, no. 10, pp. 1517–1525, 2002.

[41] X. Zhang, H. Xie, M. Hu, H. Bao, S. Yue, G. Qin, and G. Su, "Thermal conductivity of silicene calculated using an optimized stillinger-weber potential," *Physical Review B*, vol. 89, no. 5, p. 054310, 2014.

[42] W. Xu, L. Zhu, Y. Cai, G. Zhang, and B. Li, "Direction dependent thermal conductivity of monolayer phosphorene: Parameterization of stillinger-weber potential and molecular dynamics study," *Journal of Applied Physics*, vol. 117, no. 21, 2015.

[43] Y.-P. Zhou and J.-W. Jiang, "Molecular dynamics simulations for mechanical properties of borophene: parameterization of valence force field model and stillinger-weber potential," *Scientific reports*, vol. 7, no. 1, p. 45516, 2017.

[44] W. H. Moon and H. J. Hwang, "A modified stillinger–weber empirical potential for boron nitride," *Applied surface science*, vol. 239, no. 3-4, pp. 376–380, 2005.

[45] J.-W. Jiang and Y.-P. Zhou, "Parameterization of stillinger-weber potential for two-dimensional atomic crystals," *arXiv preprint arXiv:1704.03147*, 2017.

[46] M. Wen, S. N. Shirodkar, P. Plecháč, E. Kaxiras, R. S. Elliott, and E. B. Tadmor, "A force-matching Stillinger-Weber potential for MoS2: Parameterization and Fisher information theory based sensitivity analysis," *Journal of Applied Physics*, vol. 122, p. 244301, 12 2017.

[47] A. Mobaraki, A. Kandemir, H. Yapicioglu, O. Gülseren, and C. Sevik, "Validation of inter-atomic potential for ws2 and wse2 crystals through assessment of thermal transport properties," *Computational Materials Science*, vol. 144, pp. 92–98, 2018.

[48] A. Kandemir, H. Yapicioglu, A. Kinaci, T. Çağın, and C. Sevik, "Thermal transport properties of mos2 and mose2 monolayers," *Nanotechnology*, vol. 27, p. 055703, jan 2016.

[49] M. K. Transtrum, B. B. Machta, and J. P. Sethna, "Geometry of nonlinear least squares with applications to sloppy models and optimization," *Phys. Rev. E*, vol. 83, p. 036701, Mar 2011.

[50] H. Aguiar e Oliveira Junior, L. Ingber, A. Petraglia, M. Rembold Petraglia, and M. Augusta Soares Machado, *Adaptive Simulated Annealing*, pp. 33–62. Berlin, Heidelberg: Springer Berlin Heidelberg, 2012.

[51] J. Kennedy and R. Eberhart, "Particle swarm optimization," in *Proceedings of ICNN'95 - International Conference on Neural Networks*, vol. 4, pp. 1942–1948 vol.4, 1995.

[52] J. Kennedy, "The particle swarm: social adaptation of knowledge," in *Proceedings of 1997 IEEE International Conference on Evolutionary Computation (ICEC '97)*, pp. 303–308, 1997.

[53] Y. Shi and R. Eberhart, "A modified particle swarm optimizer," in *1998 IEEE International Conference on Evolutionary Computation Proceedings. IEEE World Congress on Computational Intelligence (Cat. No.98TH8360)*, pp. 69–73, 1998.

[54] Y. Karaaslan, H. Yapicioglu, and C. Sevik, "Assessment of thermal transport properties of group-iii nitrides: A classical molecular dynamics study with transferable tersoff-type interatomic potentials," *Phys. Rev. Appl.*, vol. 13, p. 034027, Mar 2020.

[55] F. Müller-Plathe, "A simple nonequilibrium molecular dynamics method for calculating the thermal conductivity," *The Journal of Chemical Physics*, vol. 106, pp. 6082–6085, 04 1997.

[56] P. K. Schelling, S. R. Phillpot, and P. Keblinski, "Comparison of atomic-level simulation methods for computing thermal conductivity," *Phys. Rev. B*, vol. 65, p. 144306, Apr 2002.

[57] R. Kubo, "Statistical-mechanical theory of irreversible processes. i. general theory and simple applications to magnetic and conduction problems," *Journal of the Physical Society of Japan*, vol. 12, no. 6, pp. 570–586, 1957.

[58] J. Ziman, *Electrons and Phonons: The Theory of Transport Phenomena in Solids*. Oxford University Press, 02 2001.

[59] W. Li, J. Carrete, N. A. Katcho, and N. Mingo, "Shengbte: A solver of the boltzmann transport equation for phonons," *Computer Physics Communications*, vol. 185, no. 6, pp. 1747–1758, 2014.

[60] P. Giannozzi, S. Baroni, N. Bonini, M. Calandra, R. Car, C. Cavazzoni, D. Ceresoli, G. L. Chiarotti, M. Cococcioni, I. Dabo, A. D. Corso, S. de Gironcoli, S. Fabris, G. Fratesi, R. Gebauer, U. Gerstmann, C. Gougoussis, A. Kokalj, M. Lazzeri, L. Martin-Samos, N. Marzari, F. Mauri, R. Mazzarello, S. Paolini, A. Pasquarello, L. Paulatto, C. Sbraccia, S. Scandolo, G. Sclauzero, A. P. Seitsonen, A. Smogunov, P. Umari, and R. M. Wentzcovitch, "Quantum espresso: a modular and open-source software project for quantum simulations of materials," *Journal of Physics: Condensed Matter*, vol. 21, p. 395502, sep 2009.

[61] M. van Setten, M. Giantomassi, E. Bousquet, M. Verstraete, D. Hamann, X. Gonze, and G.-M. Rignanese, "The pseudodojo: Training and grading

a 85 element optimized norm-conserving pseudopotential table," *Computer Physics Communications*, vol. 226, pp. 39–54, 2018.

[62] A. Togo, L. Chaput, T. Tadano, and I. Tanaka, "Implementation strategies in phonopy and phono3py," *J. Phys. Condens. Matter*, vol. 35, no. 35, p. 353001, 2023.

[63] A. Togo, "First-principles phonon calculations with phonopy and phono3py," *J. Phys. Soc. Jpn.*, vol. 92, no. 1, p. 012001, 2023.

[64] W. Li, L. Lindsay, D. A. Broido, D. A. Stewart, and N. Mingo, "Thermal conductivity of bulk and nanowire $mg_2si_xsn_1$-x alloys from first principles," *Phys. Rev. B*, vol. 86, p. 174307, 2012.

[65] A. P. Thompson, H. M. Aktulga, R. Berger, D. S. Bolintineanu, W. M. Brown, P. S. Crozier, P. J. in 't Veld, A. Kohlmeyer, S. G. Moore, T. D. Nguyen, R. Shan, M. J. Stevens, J. Tranchida, C. Trott, and S. J. Plimpton, "LAMMPS - a flexible simulation tool for particle-based materials modeling at the atomic, meso, and continuum scales," *Comp. Phys. Comm.*, vol. 271, p. 108171, 2022.

[66] J. M. Skelton, L. A. Burton, S. C. Parker, A. Walsh, C.-E. Kim, A. Soon, J. Buckeridge, A. A. Sokol, C. R. A. Catlow, A. Togo, and I. Tanaka, "Anharmonicity in the high-temperature *cmcm* phase of snse: Soft modes and three-phonon interactions," *Phys. Rev. Lett.*, vol. 117, p. 075502, Aug 2016.

Appendix A

Crystal structure modulation using phonon mode eigenvectors

When the eigenvectors $W_{\lambda,j}$ of a phonon mode $\lambda \equiv (\vec{q}, \text{branch}\{p\})$ is used to modulate basis atom j in supercell l, the displacement $u_{j,l}$ is given by

$$u_{j,l} = \frac{1}{\sqrt{n_a m_j}} \text{Re}\left[\sum_{\lambda} Q_\lambda W_{\lambda,j} \exp(i\vec{q} \cdot \vec{r}_{j,l}) \right] \tag{A.1}$$

where n_a is the number of atoms in the supercell, m_j is the mass of basis atom j, Q_λ is the displacement amplitude, $\vec{q}$ is the reduced coordinates of the phonon vector and $\vec{r}_{j,l}$ is the position of the atom. The energy of the system is calculated with the modulated atoms in the supercell frozen in [66]. The modulations of the crystal structure can easily be calculated using phonopy code [62].

Appendix B

Illustration of Vacancy Defects

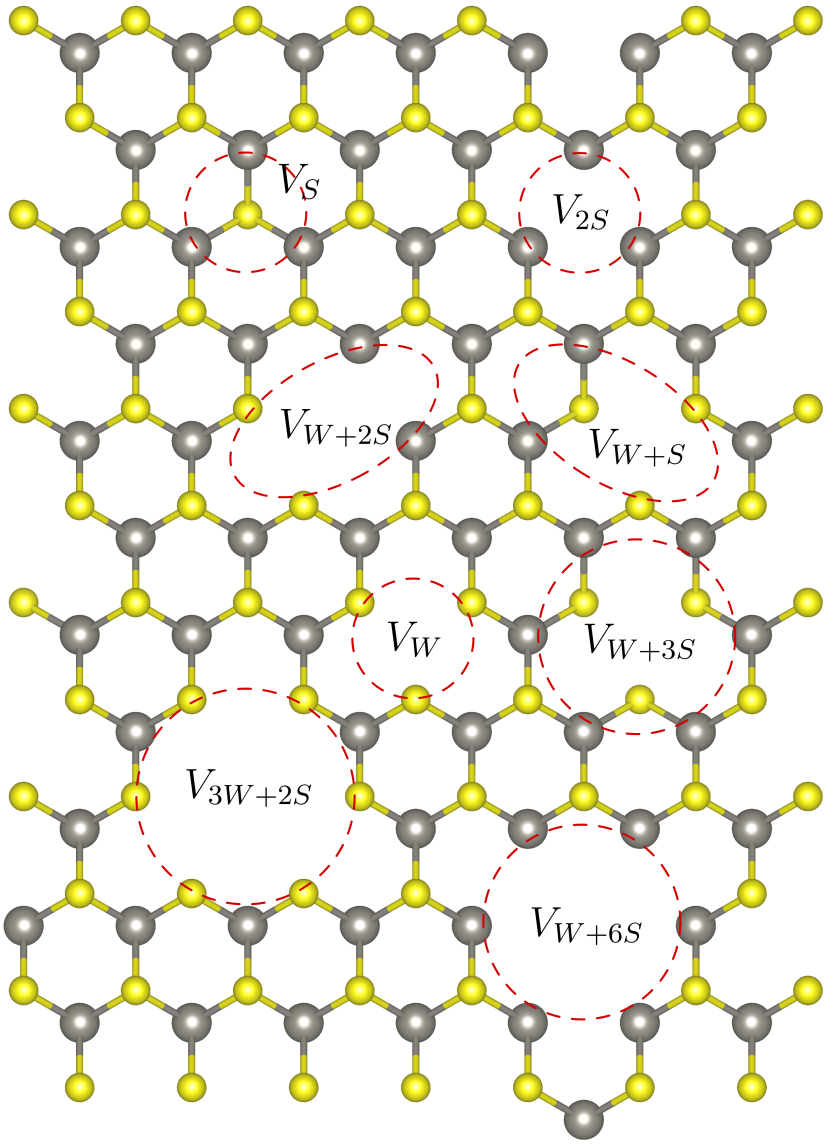

Figure B.1: 1H-WS_2 Vacancy defects considered for fitting

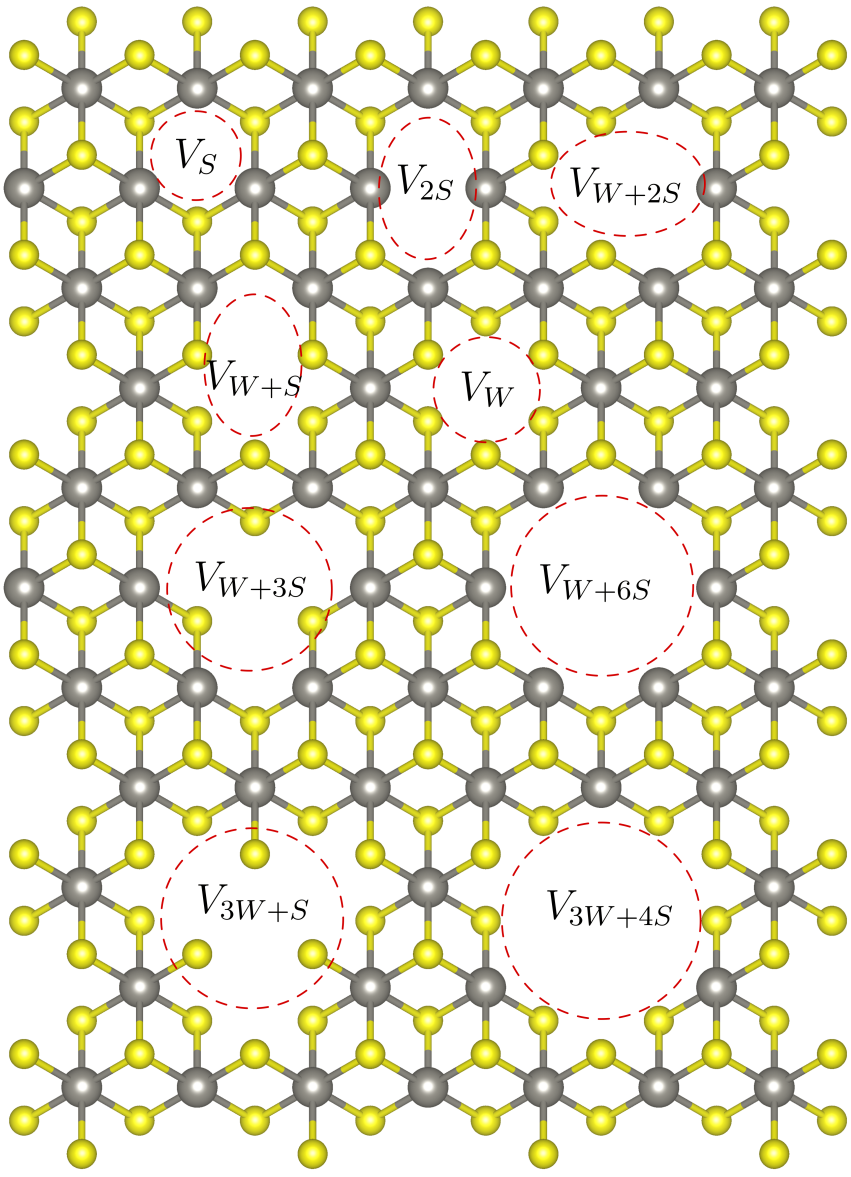

Figure B.2: 1T-WS_2 Vacancy defects considered for fitting

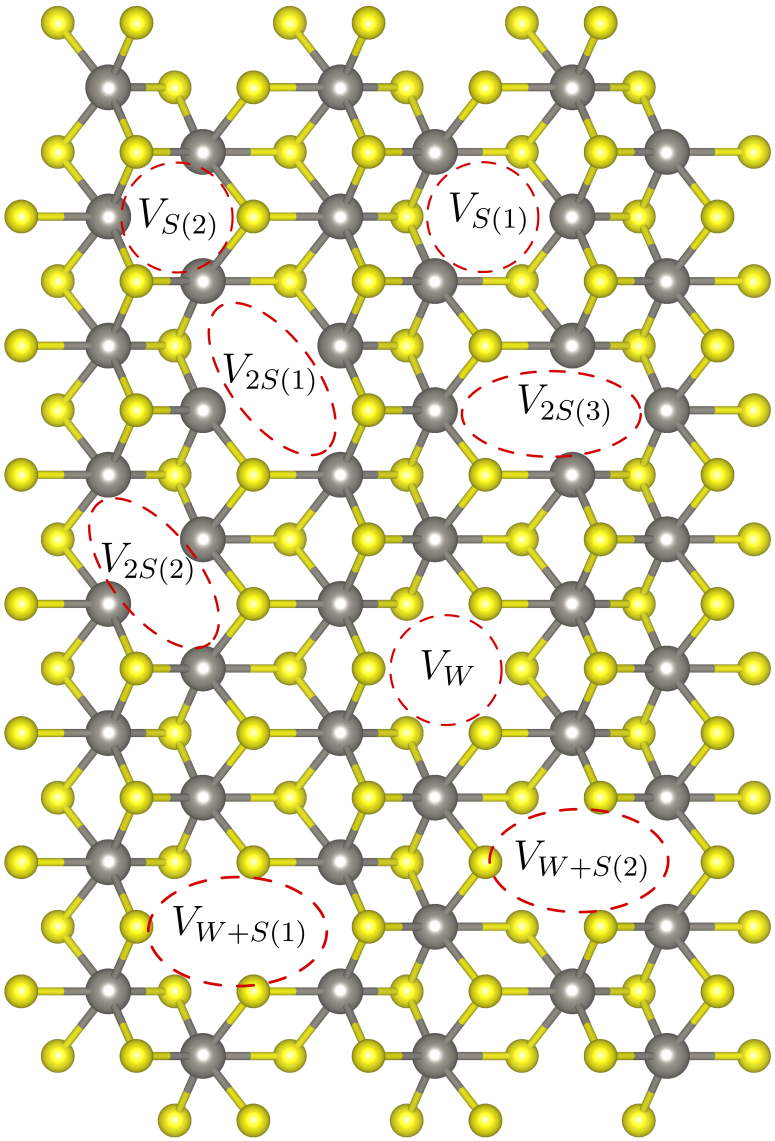

Figure B.3: 1T′-WS_2 Vacancy defects considered for fitting